Catalysis Letters (2024) 154:3976–3988
https://doi.org/10.1007/s10562-024-04596-z

Hydrogenation Synthesis of Sub-stoichiometric Tungsten Oxide (WO_X) Nanoparticles and Its Superior Decompose Rhodamine B Behavior

Osi Arutanti[1,3] · Aditya Farhan Arif[2,3] · Takashi Ogi[4] · Kikuo Okuyama[4]

Received: 25 May 2023 / Accepted: 12 January 2024 / Published online: 28 February 2024

Abstract

A metal-free, sub-stoichiometric tungsten oxide (WO_X) photocatalyst has been successfully prepared by hydrogenating WO_3 plasma nanoparticles at 425 °C. X-ray diffraction (XRD) analysis indicated that the photocatalyst comprised WO_3 monoclinic, $WO_{2.9}$, $WO_{2.7}$, and $WO_{2.0}$, depending on the reduction time. Their adsorption and photocatalytic activity on organic contaminants were evaluated by decomposing Rhodamine B (RhB). The prepared WO_X demonstrated remarkable capabilities in decomposing 1.2 gL^{-1} Rhodamine B (RhB) compared to WO_3 plasma NPs. $WO_{X\text{-}120}$ exhibited the optimal catalytic performance, with the adsorption capacity for RhB at 174.9 mgg^{-1}, 73 times greater than WO_3 plasma NPs. $WO_{X\text{-}60}$ exhibited the highest photodecomposition rate, with a k rate more than 90 times greater than that of WO_3 plasma NPs. The investigation into active species in the photocatalytic reaction suggested that superoxide hydroxyl radicals (*OH) and photoinduced holes (h^+) were the primary contributors. Furthermore, the photocatalytic degradation of RhB by the synthesized WO_X showed improvement when Benzoquinone was introduced into the system as a scavenger, effectively capturing generated electrons and inhibiting their recombination with holes. This research showed the potential for metal-free semiconductor photocatalysts to efficiently remove various organic pollutants through adsorption and photocatalysis under visible light irradiation. Furthermore, the simple reduction process makes this material promising for large-scale catalyst and photocatalyst production.

Graphical Abstract

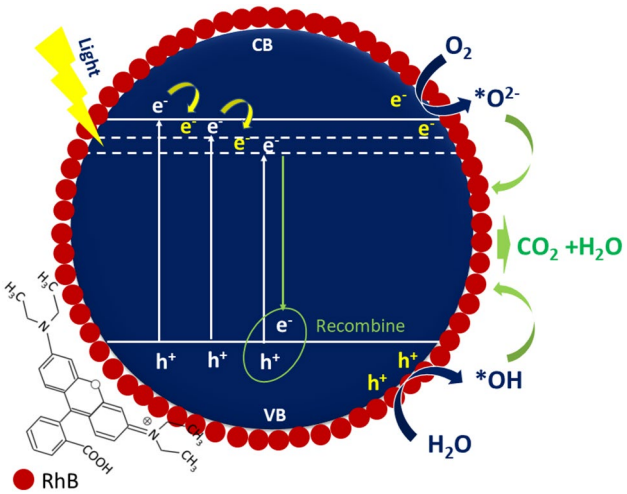

Keywords Tungsten blue oxide · Photocatalyst · Organic Pollutant · Water treatment

Extended author information available on the last page of the article

1 Introduction

The extensive utilization of dyes across various sectors like textiles, printing, and manufacturing has given rise to notable environmental detention, particularly concerning organic dye pollutants. The inappropriate disposal and insufficient treatment of these pollutants resulted in the pollution of ecosystems. The long-term negative impacts on human health, animals, and the environment must be addressed promptly[1, 2]. As a result, wastewater technology has evolved into an increasingly critical challenge. The development of wastewater treatment and rehabilitation technologies prior to disposal has been extensively pursued through physical, chemical, and biological methods[3–6]. Among the wastewater treatment technologies, the advanced oxidation process, i.e. photocatalysis, has been an intensive research subject over the past few decades. Unlike conventional methods, photocatalysis employs the energy from photon energy, sunlight, to trigger chemical reactions that effectively decompose and neutralize organic pollutants[7–9].

Metal oxide-based photocatalytic materials, tungsten oxide (WO_3) is recognized as a highly promising material due to its remarkable physicochemical characteristics. The low band gap energy value (ranging from 2.6 to 2.8 eV), making this material could be activated under visible light directly compared to the common photocatalyst titanium dioxide (TiO_2)[10, 11]. However, WO_3 demonstrates slightly lower efficiency due to variations in the valence band position.

Principally, the fundamental photocatalytic process involves absorbing light energy, which generates excited electrons, giving rise to superoxide anions (O_2^-) and hydroxyl radicals (OH*). These radicals catalyze the breakdown of pollutants into H_2O and CO_2 molecules due to their elevated potential energy. However, a challenge arises in the rapid recombination of electron–hole pairs, which diminishes photocatalytic efficiency[8, 12]. To overcome the disadvantages, co-catalyst materials like semiconductors, metals, carbon-based substances, and polymers intervene to prevent the recombination[13–17]. Integrating expensive metal dopants significantly impacts the photocatalytic process[14, 18]. However, widespread use of precious metals can escalate production costs.

Moreover, metal oxides have the potential to serve as advanced adsorbents due to their lower regeneration temperature compared to activated carbon[10, 19, 20]. Unfortunately, their adsorption capacity is lower, and ongoing efforts are being made to improve it. Combining WO_3 with carbon-based materials can enhance the absorption capability of organic pollutants. However, the adsorption capacity gradually decreases over time and reached saturation, necessitating additional treatments to remove or clean the organic impurities on the carbon-based material surfaces [15, 21–23].

Modifying the structure of tungsten oxide through various oxygen-deficient stoichiometries (WO_{3-x}) presents another possibility to enhance its adsorption capacity [24–27]. Several techniques have been proposed for manipulating oxygen deficiencies. Shen et al. [28] utilized an evaporation process to produce WO_{3-x}. However, a high-temperature treatment exceeding 800 °C is needed to generate nanorod WO_x. Li et al. [29] and Shang et al. [24] proposed the hydrothermal synthesis of $W_{18}O_{49}$, which conducts at lower temperatures, but requires a long synthesis process of over 12 h. Chemical reduction was also employed by Chen et al. [30] to produce WO_x. Among the research reports showed that hexagonal WO_3 nanorods and nanotube bundles with unsaturated W atoms exhibit higher adsorption abilities for organic dyes than monoclinic structures. Additionally, sub-stoichiometric tungsten oxide (WO_X) possesses catalytic and adsorbing properties due to oxygen vacancies leading to better performance relative to WO_3[25, 31–34]. Nevertheless, there are examples where the introduction of additional metals becomes necessary to decompose higher concentrations of organic dye pollutants effectively.

In our previous research, we successfully synthesized WO_X nanoparticles by using a convenient one-step hydrogenation method [35]. By varying the reduction temperature from 300 to 700 °C and demonstrated the effectiveness of metal-free semiconductor-based photocatalytic materials in decomposing high concentrations of Rhodamine B through a single process. The result showed that the optimum temperature to was at a low reduction temperature of 425°C. Interestingly, our results showed high catalytic activity without visible light compared to other research reports on adsorption and photocatalytic activity to decompose concentrated Rhodamine B. Developing sub-stoichiometric WO_3 materials holds immense potential for large-scale applications. Accordingly, advancing sub-stoichiometric WO_3 materials opens up significant possibilities for broad-scale applications.

Continuing in this line of research, the present study aims to explore the effect of reduction time on the characteristics of the prepared WO_X from 30 to 180 min, specifically focusing on its adsorption and photodegradation capabilities under simulated solar irradiation. The current research findings suggest that the slightly changing reduction time at the optimal reduction temperature (425 °C) influenced the physicochemical properties significantly, especially in the adsorption and photodegradation activity.

2 Experimental

2.1 Preparation of WO_X Nanoparticles

Substoichiometric tungsten oxide (WO_X) was obtained by hydrogenating plasma-synthesized NPsWO_3 plasma NPs (6 nm in size, Nishin Engineering Inc., Japan) without additional treatment. The WO_3 plasma NPs were subjected to calcination at 425 °C in an electric vacuum furnace, with an H_2 gas flow rate of 1 $Lmin^{-1}$, for different reduction times ranging from 30 to 180 min. Prior to the reduction process, the oxygen content in the tubular reactor was minimized by evacuating the air and filling the reactor with high-purity H_2. This study represents a continuation of previous research investigating the impact of reduction time on the process [35].

2.2 Characterization of Physical Properties

X-ray diffraction (XRD, Bruker D2, Cu Kα radiation, and a LinkEye detector Japan) was utilized to analyze the crystal structure of the prepared WO_X. RAMAN spectrometer (iHR320 HORIBA, Japan) was employed to study the chemical vibration. Particle morphology was evaluated using High-Resolution Transmission Electron Microscopy (HRTEM, JEM-3000F, Japan). Optical properties were studied using DR-UV. The binding energies around the O1s orbit were observed using XPS measurements (ESCA-3400, Shimadzu Corporation, Japan).

2.3 Adsorption and Photodegradation Performance Analysis

In a typical experiment, 100 mg of catalyst was dispersed into 200 ml of 1.2 gL^{-1} Rhodamine B (RhB, Wako Pure Chemical Industries Ltd., Japan) as the waste model dye organic pollutant. The solution was stirred intensely under dark conditions for 3 h and sampled regularly. The adsorption amount of the prepared WO_X to RhB was calculated from Eq. 1 as follows [36]:

$$q_t = \frac{(C_0 - C_t)V}{m} \quad (1)$$

where q_t is the amount of RhB adsorbed at time t(min), C_0 (mgL^{-1}) is the initial RhB concentration, C_t (mgL^{-1}) is the solution concentration at time (min), V (L) is the solution volume, and m (g) is the quality of the adsorbent.

After reaching the equilibrium, the photocatalytic activity was measured for 2 h under simulated solar light (PEC-L11, Peccell Technologies Inc., Japan) at room temperature while introducing O_2 gas at a flow rate of 0.5 $Lmin^{-1}$ to maintain dissolved O_2 concentration. Samples were collected at specific times, centrifuged, and analyzed using a UV–Vis spectrophotometer (UV-3150, Shimadzu, Japan). Using a similar step, 30 ppm of Tetracycline (pharmacy medicine) and Ciprofloxacin (pharmacy medicine) were used as the pharmaceutical pollutant waste model. The medicine is ground finely, then weighed and mixed into water. The optimum condition of WO_X was used as the catalyst.

Cyclic photocatalysis tests were conducted using $WO_{X\text{-}60}$ and repeated five times. Following each Rhodamine B degradation cycle, the catalyst was separated from the solution through centrifugation and subjected to two washes with H_2O and ethanol. Subsequently, the catalyst was dried at 100 °C overnight and reused in the subsequent cycles[35].

Scavenger experiments examined the active species generated during the photocatalytic process. Iso Propanol (IPA), Ammonium Oxalate (AO), and Benzoquinone (BQ) were introduced as scavengers into the system to capture hydroxyl radicals (*OH), photoinduced holes (h^+), and superoxide radicals ($*O_2^-$), respectively. The methodology was adapted from previous research[37].

3 Result and Discussion

The observed color change indicates a possible crystal structure and phase transition alteration. X-ray diffraction (XRD) patterns of the prepared WOx at various reduction times were examined within 2θ angles from 20° to 80° [38]. Notably, a significant peak shift occurred between 20 and 40° (Fig. 1a), and peaks corresponding to $WO_{2.0}$, $WO_{2.7}$, and $WO_{2.9}$ were observed and denoted by the symbols. The diffraction peaks of plasma-synthesized WO_3 nanoparticles (NPs) could be accurately indexed to a monoclinic structure (JCPDS: 43–1035) when 2θ at 23.6° and 24.7° [24, 35]. Considering that the color of the oxide was dependent on the oxidation state of tungsten due to oxygen loss, which generates additional states such as W^{5+}, W^{4+}, or a mixture of W^{6+} and W^{5+}, it is believed that longer reduction times lead to more oxygen vacancies on the tungsten surface [32, 39, 40]. Consequently, the stability decreased, and the surface layer easily reoxidation upon exposure to air. As a result, $WO_{X\text{-}180}$ exhibited a brighter blue color and a similar phase structure to that of WO_3 plasma NPs, suggesting that the oxygen vacancy affected the electronic property and its light adsorption NPs. The results demonstrated that the current process has successfully generated oxygen vacancies by varying reduction times.

In order to gain a more in-depth understanding, X-ray photoelectron spectroscopy (XPS) was employed to investigate the surface oxygen vacancies at the O1s orbital in $WO_{X\text{-}60}$ (Fig. 1b). The analysis unveiled three distinct peaks at binding energies (BEs) of 530, 531.9, and 533.3 eV,

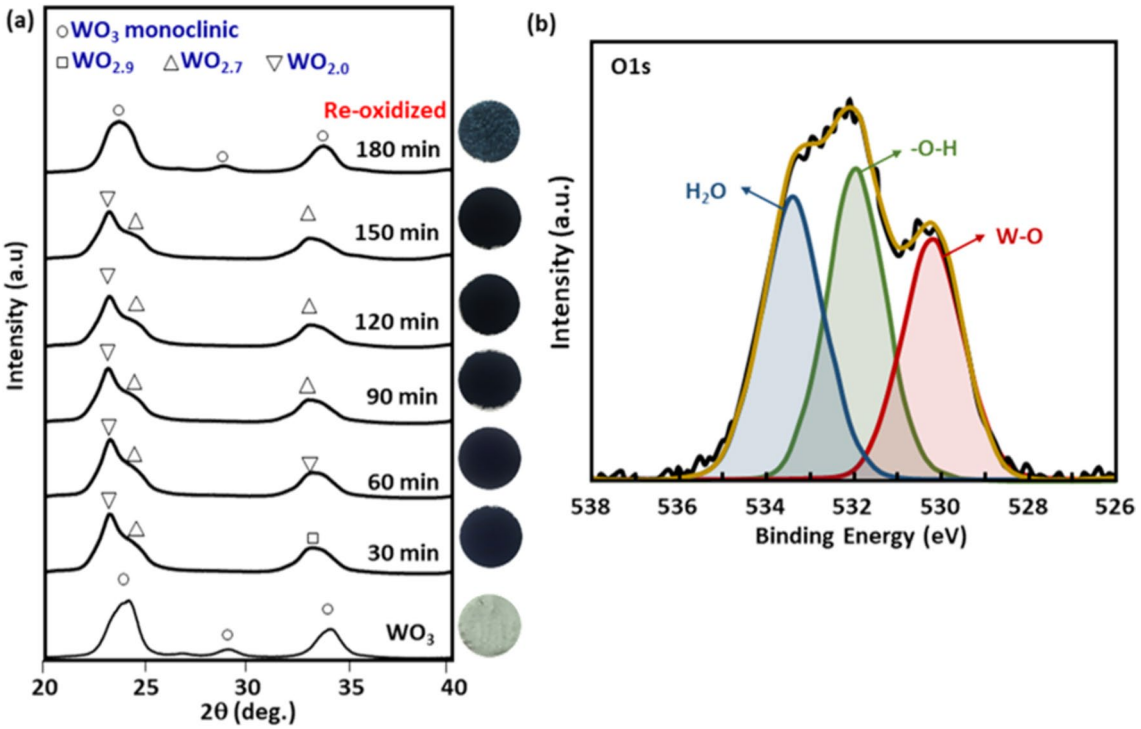

Fig. 1 X-ray diffraction spectra of WO_3 plasma NPs and the prepared WO_X (**a**), and O1s X-ray photoelectron spectra of $WO_{X\text{-}60}$ (**b**)

corresponding to W–O bonds, oxygen atoms near oxygen vacancies, and OH bonds, respectively. This finding holds significant importance since the XPS O1s peak of WO_3 exhibits only two binding energies (530 and 533 eV), confirming the presence of oxygen-deficient compounds in the prepared WO_X [39, 40]. The existence of OH bonds can be attributed to moisture absorption. Furthermore, the higher peak intensity at 531 compared to 530 suggests that the hydrogenation process resulted in more noticeable oxygen vacancies than WO_3 plasma NPs.

Figure 2. displays the characterization of the samples using RAMAN spectroscopy, which revealed three prominent vibration bands at 272, 716, and 807 cm^{-1}. These bands can be attributed to the bending vibration of δ (O-W-W) and the stretching vibration of δ (W–O–W). These results was also similar to other reported [11, 34, 38]. Broadening and lowering of the Raman peaks indicated an increase in disordered regions, particularly when the reduction time was extended from 30 to 90 min. Beyond 90 min, the Raman peak at 807 cm^{-1} became more prominent and sharper, supporting the observed reoxidation process in the XRD results. The peak characteristic of $WO_{X\text{-}120}$ was also similar to WO_3 plasma NPs. An intriguing small peak at around 950 cm^{-1} was also detected and identified as the $W^{5+}=O$ bond resulting from an oxygen vacancy.

The UV diffuse reflectance spectroscopy results, as shown in Fig. 3 illustrate the absorption characteristics of WO_3 plasma NPs and the prepared WO_X samples. They observed that increasing reduction time leads to a decrease in the absorption intensity of the prepared catalyst. The band gap energy was determined by extrapolating the Kubelka–Munk unit vs. photon energy plots [40]. It was observed that the band gap energy of WO_3 plasma NPs was approximately 2.8 eV (700 nm), similar to commercially available WO_3. However, the reduction process led to a decrease in the band gap energy. Within 30–150 min, the band gap energy remained relatively constant at 2.6 eV.

Nevertheless, beyond 150 min, the band gap energy decreased to 2.3 eV. Based on the band gap energy, the prepared WOx exhibited adsorption in near-infrared (NIR) over 600 nm. Notably, the reoxidation process only influenced the change in particle color and phase structure while not impacting the optical properties. The above findings indicated a direct correlation between the degree of oxygen vacancy and the decrease in the band-gap of tungsten oxides. As a result of their enhanced absorption capabilities within the visible spectrum, it can be inferred that all the prepared WO_X materials will exhibit superior photocatalytic properties for the decomposition of RhB compared to WO_3 plasma NPs.

According to the findings presented in Fig. 4, the morphology and size of the prepared WO_X remain unchanged when compared to the original WO_3 plasma NPs. Furthermore, the high-resolution transmission electron microscopy

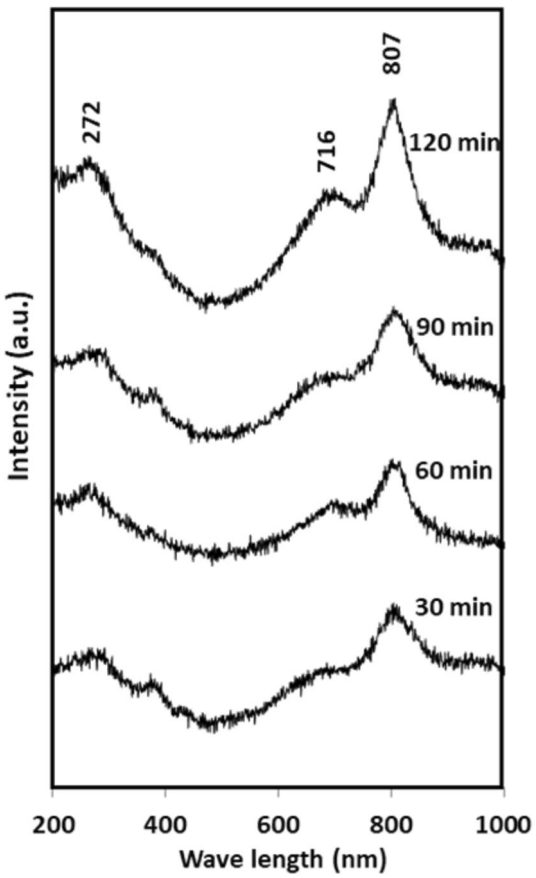

Fig. 2 Raman spectra of the prepared WO_X

(HRTEM) analysis further confirmed that the prepared WO_X exhibited a well-defined crystal structure, with consistent lattice fringes observed at 2.6 Å. These fringes can be attributed to the (110) and (200) planes of tungsten oxide, indicating the successful formation of WO_X with high crystallinity. Defect crystal as the effect of oxygen vacancy could be observed by red circle.

Before initiating the photodegradation process, 3 h were allocated for achieving the adsorption–desorption equilibrium of WO_3 plasma nanoparticles and the prepared WOx on the photocatalyst without visible light. The preliminary focus was on examining the adsorption properties of the synthesized WO_X, with results presented in Fig. 5a-b. From Fig. 5a, obviously that the adsorption equilibrium was established within the initial 10-min interval. Notably, the adsorption rate during this period displayed an inversely proportional with the duration of reduction time. The longer the reduction time, the slower the adsorption rate within the initial 10 min. Specifically, WO_3 plasma nanoparticles exhibited the weakest adsorption efficiency, with only a about 10% decomposition of RhB. Significantly, WO_{X-30}, and WO_{X-60} demonstrated a relatively swift attainment of adsorption equilibrium, showcasing a gradual reduction in RhB concentration to 47.6 and 134.7 mgg^{-1}, respectively. As the reduction times increased, a discernible impact on adsorption activity emerged, delineating distinct adsorption curve patterns for various structures (Fig. 5b). Particularly, WO_{X-30} and WO_{X-60} depicted a similar trend, with WO_{X-60} manifesting the highest adsorption rate within 10 min. While the initial adsorption rate of other WO_X variants below than WO_{X-60}, their overall adsorption efficiency still reached 92% for RhB within 3 h.

Despite the similar specific surface area of WO_3 and reduced WO_3 [35], the increased activity may be attributed to enhanced surface catalyst stability due to more oxygen vacancies. When the reduction time was over 60 min, the adsorption equilibrium time lasted almost 2 h. WO_{X-90}, WO_{X-120}, and WO_{X-180} adsorption capacities reached 148, 175, and 183 mgg^{-1}, respectively. The oxygen vacancies provided the adsorption sites. Throughout the process, dye molecules adhere to the particle surface, forming clusters that create a steric hindrance. This hindrance restricts the diffusion and penetration of additional dye molecules from the external to the internal surface[24, 32, 40]. Consequently, the amount of adsorbed dye reaches a near-constant level at a specific time. Hence, the varying adsorption rates observed within the initial 10 min can be attributed to the influence of reduction time on the surface structure and chemical properties of the synthesized WO_X.

Since the concentration of RhB almost 100% adsorbed by WO_{X-120} and WO_{X-180}, the photocatalytic phenomenon will be focusing on the WO_3 plasma NPs and reduced WO_3 until 90 min. Compared to its adsorption performance, the photocatalytic activity of RhB under visible light irradiation for 2 h was relatively lower (Fig. 6). Interestingly, there was no observable photodegradation of RhB over WO_3 plasma NPs. However, as with the adsorption phenomenon, the photodegradation of RhB significantly increased with longer reduction times obviously. During the 2 h irradiation, the photodegradation efficiencies of RhB over WO_{X-30}, WO_{X-60}, and WO_{X-90} were approximately 2%, 6%, 40%, and 35%, respectively (Fig. 6a). The correlation between -Ln(C/C0) and irradiation time during the process is shown in Fig. 6b, enabling the calculation of rate constant (k) values for the photodegradation reactions. The rate constant of the photodegradation reaction of RhB over WO_3 plasma NPs was found to be the smallest at 0.08×10^{-3} min^{-1}. Comparatively, the previous study reported a photodegradation rate of WO_3 plasma NPs was 2.98×10^{-3} min^{-1} for 0.2 mgL^{-1} RhB, indicating the significant influence of catalyst quantity and RhB concentration on photocatalytic activity [35]. The rate constants for the photodegradation reaction of RhB using WO_{X-30}, WO_{X-60}, and WO_{X-90}, were 0.68, 7.50, and 5.55×10^{-3} min^{-1}, respectively. Based on Fig. 6b, the highest rate was observed with WO_{X-60}, with a k rate more than 90 times greater than that of WO_3 plasma NPs. Based on

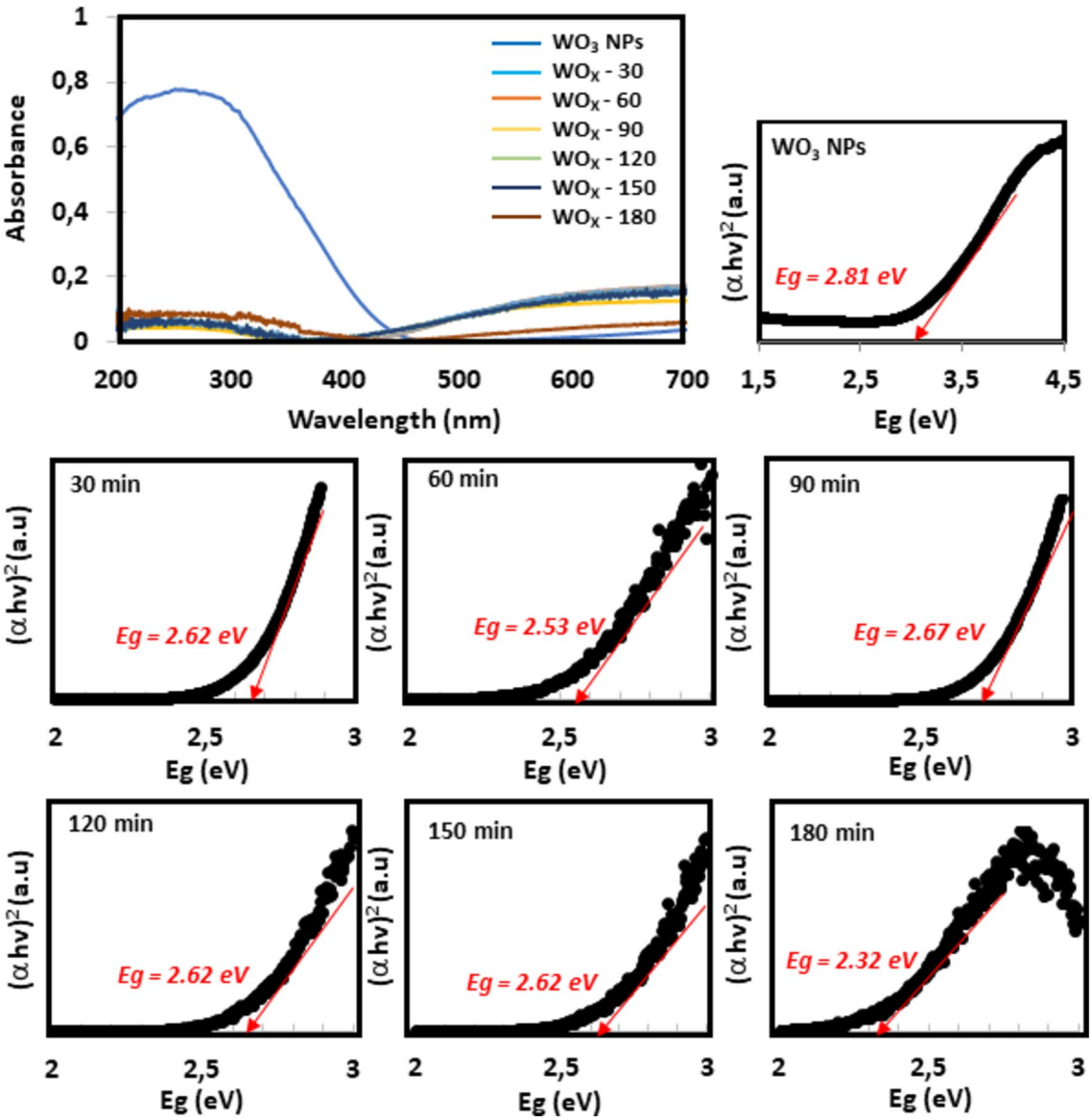

Fig. 3 The optical band gap energy of the prepared WO_X

the band gap energy values and adsorption phenomenon, it can be concluded that longer reduction times increase the number of oxygen vacancies, which leads to enhanced electron–hole recombination.

The ability of the prepared $WO_{X\text{-}60}$ as the optimum condition to decompose another organic pollutant was also tested. Ciprofloxacin (CP) and Tetracycline (TC) have been used as the pharmaceutical waste model, as shown in **Figure SI1**. Like decomposed dye pollutants (RhB), the peak of CP and TC decreased by increasing the contact time. **Figures SI1a** and **SI1b** show the CP degradation and TC degradation under visible light irradiation. Based on **Figure SI1a**, Ciprofloxacin has three absorption peaks at 270, 325, and 334 nm. The investigation of CP degradation is divided into two peak areas (insert **Figure SI1a**) showing the degradation of CP under two different wavelength ranges, 270 and 300–350 nm. The peak of 270 nm decreased almost 25% after 1 min of contact time and remained around 50%, with the peak lightly shifted to 275 nm after 3 h of dark condition. No photocatalytic activity was indicated after 2 h of illumination. In another condition, all peaks 325 and 334 decreased around 35% after 1 min of interaction and disappeared after 3 h of reaction under dark conditions. A similar trend for Tetracycline was observed. Naturally, Tetracycline has two active peaks at 280 and 360nm. Based on the small insert, **Figure SI1b** showed that all peaks of Tetracycline disappeared after 1 min of contact. Different chain structures of organic pollutants influenced the efficiency of adsorption

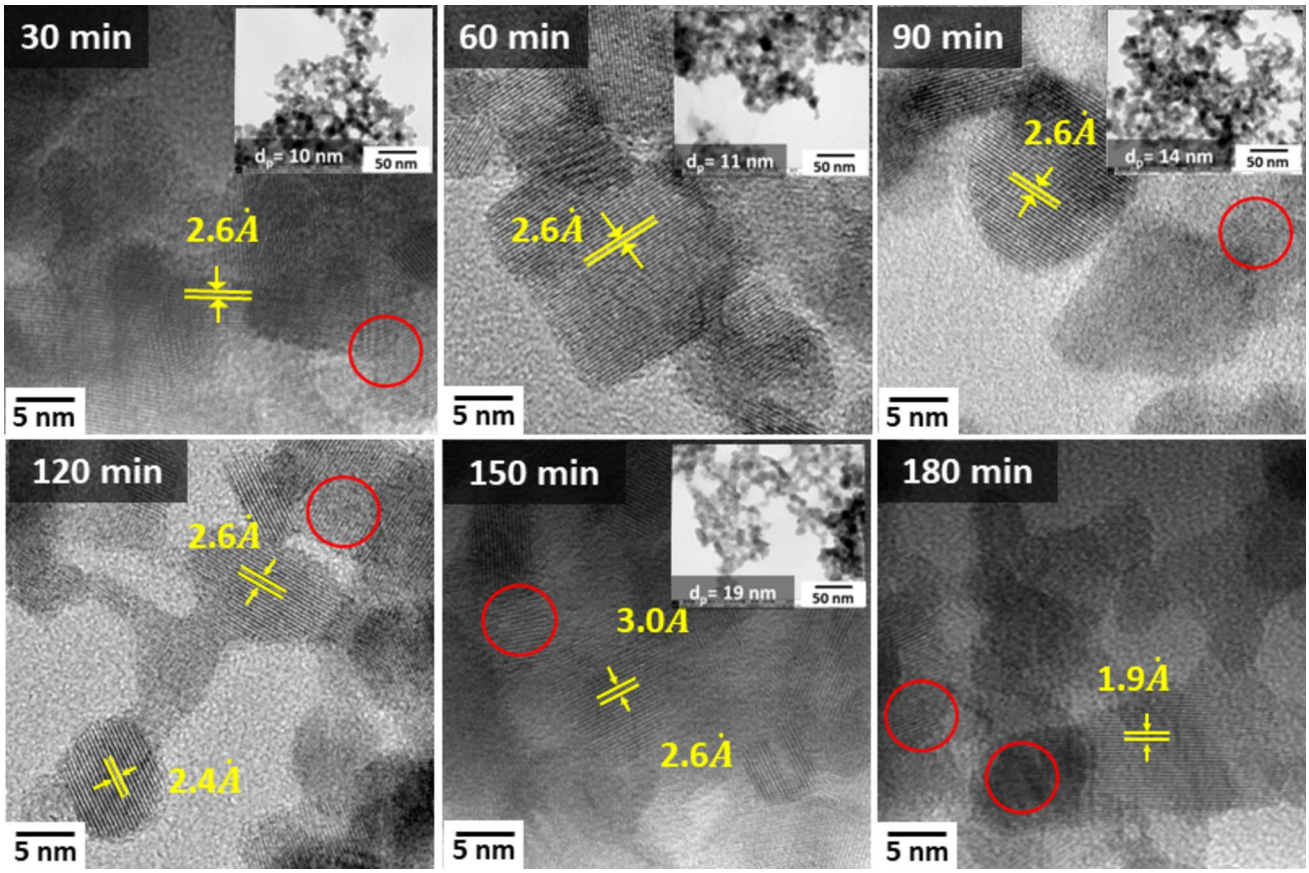

Fig. 4 The morphological characteristics and HRTEM images of the prepared WO_X

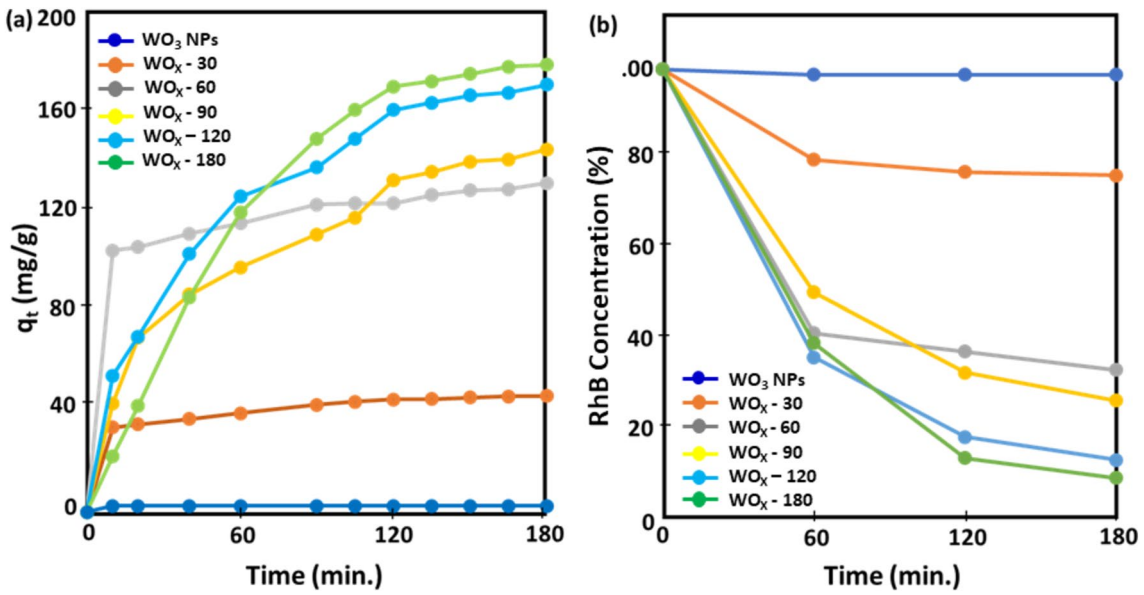

Fig. 5 Effect of contact time on the adsorption capacities of the prepared WO_X versus time (**a**), and adsorption removal profiles of Rhodamine B (**b**)

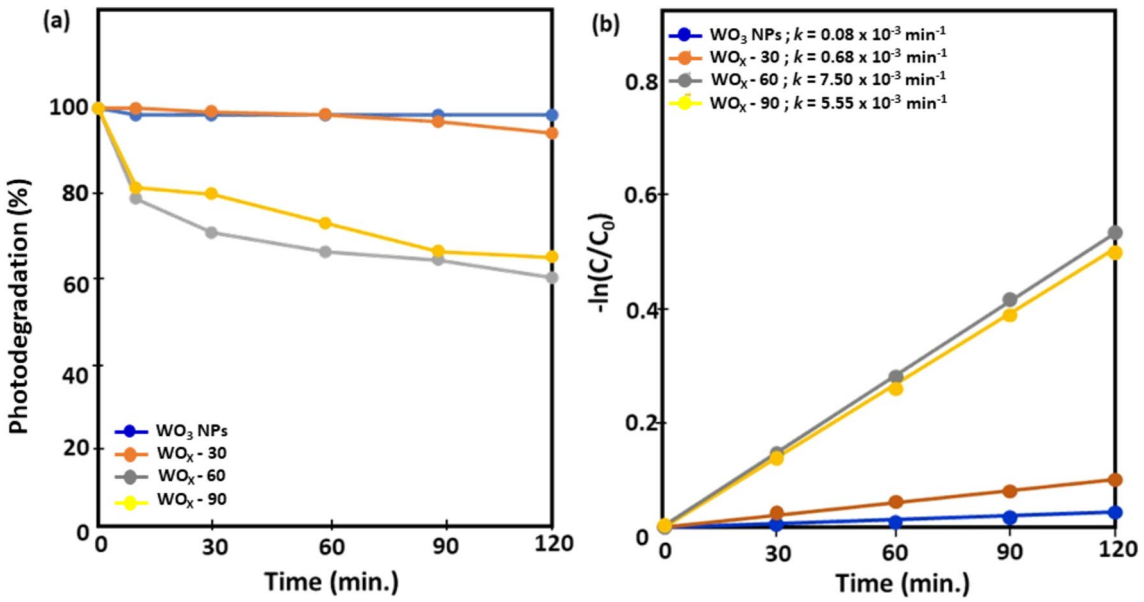

Fig. 6 Photodegradation plots of Rhodamine B over the time (**a**), and degradation kinetics plots of the prepared WO_X (**b**)

and photocatalytic. The results indicate that the current prepared WO_X has the adsorption ability to adsorb various organic pollutants at high concentrations.

Here, oxygen vacancies act as self-doping agents without introducing foreign impurity elements. These vacancies strengthen the oxygen evolution reaction (OER) and provide unsaturated sites that facilitate molecular adsorption. In line with prior research [35], oxygen vacancies impact adsorption and photocatalytic activity through their function as donor densities and sites that trap electrons, effectively impeding electron–hole recombination. The precise effects of electron traps and recombination centers on the quantity and placement of these oxygen vacancies.

The stability of $WO_{X\text{-}60}$ was corroborated through a five-times cycling test, as depicted in Figs. 7 the observed variations in the final concentration of Rhodamine B, decreasing from 80 to 65%. The activity of degradation of RhB under dark conditions after the third cycle was lower, and illumination was almost stable under light. The different activities were likely attributed to differences in the reduced catalyst amount after the initial cycle's decomposition process and the cleanness of the dye pollutant's catalytic surfaces.

Table 1 comprehensively compares optical characteristics, adsorption capabilities, and catalytic and photocatalytic activities. Generally, distinct reduction times substantially affect adsorption and photocatalytic performance. All the synthesized WO_X samples exhibited notably elevated activity in contrast to WO_3 plasma nanoparticles. This insight aligns with the color and phase alterations observed in Fig. 1a, as supported by XRD analysis. Such circumstances facilitate the generation of oxygen vacancies, which play

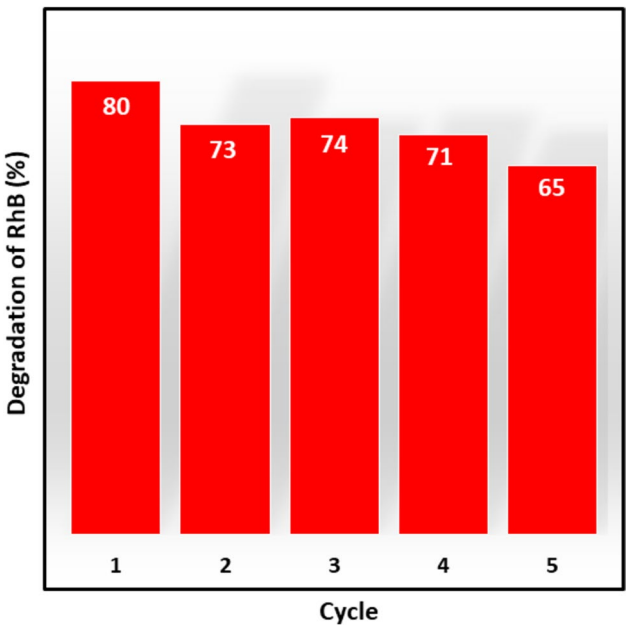

Fig. 7 Photocatalytic cycling test

an important role in RhB adsorption and photocatalytic performance.

Another approach to studying the various factors influencing photodegradation involves analyzing the active species. Moreover, Fig. 8 illustrates the evaluation of the most influential radical species during the Rhodamine B photodegradation process. The impact of these active species was assessed by observing the variation in C/C0 of RhB after

Table 1 Effect of Reduction Time on the optical, adsorption, and photocatalytic properties of the prepared WO_X

Sample	Eg (eV)	γ (%)	q_t (mgg^{-1})	k (min^{-1})
WO_3 NPs	2,81	2	2.5	0.08
$WO_{X\text{-}30}$	2,62	25	47.6	0.68
$WO_{X\text{-}60}$	2,53	67	134.7	7.50
$WO_{X\text{-}90}$	2,67	78	148.3	5,55
$WO_{X\text{-}120}$	2,62	88	174.9	-
$WO_{X\text{-}180}$	2,32	92	183	-

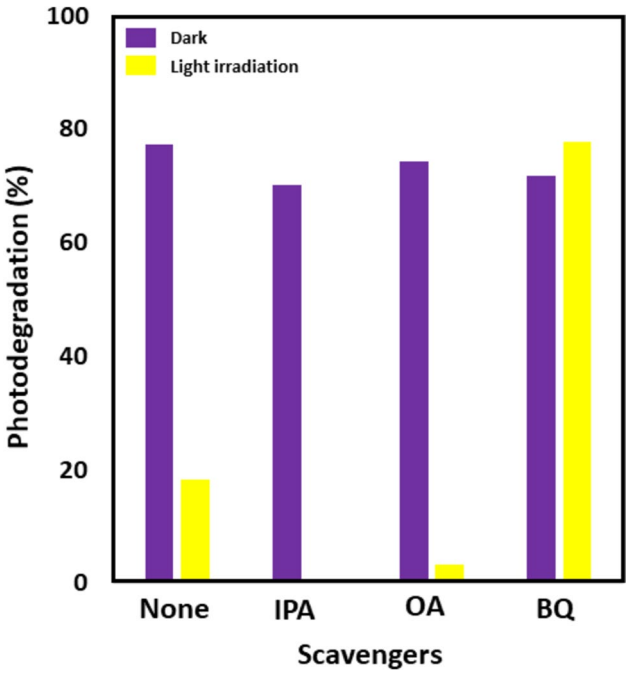

Fig. 8 Effect of active species scavengers in photodegradation of RhB

introducing scavengers into the photocatalytic system. The catalytic activity under dark conditions (violet bar) remained stable, indicating that the presence of scavenger species did not influence the catalytic activity. However, distinct results emerged under photoirradiation (yellow bar). The presence of scavengers in the photocatalytic process led to decreased activity, attributed to their reactivity with the generated radical species.

Consequently, this phenomenon reduced the number of generated radical species responsible for RhB decomposition. Adding IPA to the system resulted in almost 0% photodecomposition of RhB, significantly inhibiting its degradation compared to the 18% observed in the absence of scavengers (None). Unlike IPA, the presence of AO led to a RhB decomposition of up to 3.45%, though still considerably lower than the absence of scavengers. These results indicate that a substantial number of hydroxyl radicals (OH*) and photoinduced holes (h^+) were generated when the prepared WO_X was irradiated under solar simulator irradiation, playing a crucial role in the degradation of dyes.

Interestingly, when BQ was introduced into the system, the photodegradation of RhB evidently increased, with almost 78% of RhB decomposed, much higher than that of the absence scavengers.

Since the effectivity of the active sites is also influenced by the valence and conduction band position, the value of the valence band potential (EVB) and conduction band potential (ECB) of the prepared catalyst was also evaluated. Theoretically, the potential of the conduction band must be more damaging than the potential of the acceptor, and the potential of the valence band must be more favorable than the potential of the donor[41]. The value of EVB and ECB of the prepared WO_X was estimated by using the Mulliken electronegativity according to the following equations[42–44]:

$$EVB\left(WO_{X-60}\right) = X\left(WO_{X-60}\right) - E_C + 0.5xE_g(WO_{X-60}) \quad (2)$$

$$ECB = EVB\left(WO_{X-60}\right) - E_g(WO_{X-60}) \quad (3)$$

Ec represents the energy of free electrons on the hydrogen scale (4.5 eV), Eg is the band gap energy, and X denotes the electronegativity of the semiconductor.

$$X = \sqrt{X_W + X_O} \quad (4)$$

$$X_W = 0.5x\left(I_1 + E_1\right) \quad (5)$$

$$X_O = 0.5x\left(I_1 + E_1\right) \quad (6)$$

where X_W and X_O represent the electronegativity of Tungsten (W) and Oxygen (O) elements, respectively, determined by identifying the first ionization energy (I_1) and electron affinity (E_1) for each element. Given the values of 7.98 eV and 13.62 eV for I_1, and 0.81 eV and 1.46 eV for E_1, for W and O elements, respectively, the Mulliken electronegativity can be calculated to be approximately 5.76 eV. Consequently, the calculated values of EVB and ECB for $WO_{X\text{-}60}$, with a band gap energy of 2.53 eV (Fig. 3), are found to be 2.523 and -0.007 eV, respectively. Applying similar steps, the positions of VB and CB of the prepared catalyst can be estimated and compared with the redox potential presented in Fig. 9. The results indicate that the reduction process leads to changes in EVB and ECB.

According to the findings, the holes in the valence band exhibit a more positive potential than the potential of $*OH/OH^-$ (1.99 eV) and $*OH/H_2O$ (2.27 eV). This result aligns with the analysis of active species, where the *OH and h^+ play the leading role in the photodegradation. However, the generated electrons in the conduction band

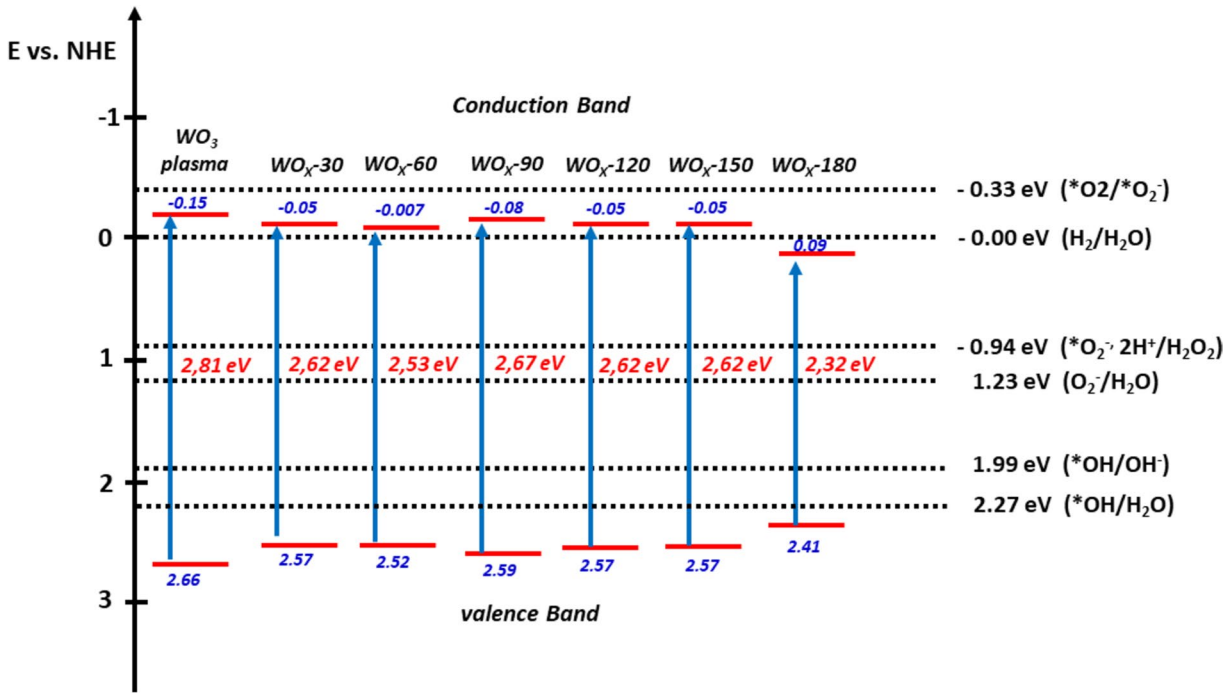

Fig. 9 Potential energy of the prepared catalysts

cannot reduce O_2 into $*O_2^-$ as an electronic acceptor due to the potential of ECB being more positive than that of $*O_2^-/O_2$ (− 0.33 eV). Consequently, under visible light irradiation, the electrons generated in the Valence Band quickly recombine with the holes in the conduction band through direct recombination and surface recombination. This leads to a reduced efficiency of the photocatalytic reaction. Nevertheless, the diverse structural mixtures in the prepared WO_X as the presence of oxygen vacancy contribute to differences in Fermi-level energy. Consequently, electrons migrate spontaneously from higher Fermi to lower energy levels, while holes move from negative to positive levels, enhancing the separation of electron–hole pairs and improving the efficiency of WO_X compared to WO_3 plasma nanoparticles.

Introducing BQ into the system as a scavenger to capture $*O_2^-$ significantly restrains the recombination of electrons and holes. BQ can accept electrons from the photocatalyst, producing a semiquinone radical (*BQ), which, upon exposure to light, forms Reactive Oxygen Species (ROS). This molecule can further react with molecular oxygen to generate BQ. This redox cycling process generates reactive oxygen species (ROS) and radicals that actively participate in the photodegradation of RhB[45].

Based on the current results, the photocatalytic mechanism of the synthesized WO_X can be succinctly described as follows:

$$WO_{3X} + h\nu \rightarrow e- + e^-_{trap} + h+ + h^+_{trap} \quad (7)$$

$$\mathrm{e-} + \mathrm{h+} \rightarrow \text{recombination} \quad (8)$$

$$h^+_{trap} + H_2O \rightarrow OH* + H^+ \quad (9)$$

$$e^-_{trap} + O_2 \rightarrow 2H^+ + *O_2- \quad (10)$$

$$2e^-_{trap} + O_2 + 2H+ \rightarrow H_2O_2 \quad (11)$$

$$H_2O_2 + e^-_{trap} \rightarrow OH\circ + OH* \quad (12)$$

$$\mathrm{H_2O_2} \rightarrow 2\mathrm{OH}* \quad (13)$$

$$e^-_{trap} + BQ \rightarrow BQ- \quad (14)$$

$$\mathrm{BQ} + *\mathrm{O_2}- \rightarrow \mathrm{BQ-} + \mathrm{O_2} \quad (15)$$

$$\mathrm{BQ-} + \mathrm{H_2O} \rightarrow \mathrm{BQ} + \mathrm{OH^-} \quad (16)$$

$$\mathrm{OH}* \text{ and } *\mathrm{O_2^-} + \mathrm{RhB} \rightarrow \text{products} \quad (17)$$

This finding aligns with the outcomes of the IPA and AO scavenger tests, highlighting the main role of holes and hydroxyl radical groups in the degradation of organic dye. Furthermore, the photocatalytic degradation of RhB by the synthesized WO_X showed improvement when Benzoquinone was introduced into the system as a scavenger, effectively capturing the generated electrons and inhibiting their recombination with holes.

The current study demonstrates that the presence of oxygen vacancies in the prepared WO_X not only significantly influences its physical properties but also imparts unique catalytic and photocatalytic properties compared to WO_3 plasma nanoparticles. The prepared WO_X demonstrated excellent potential as a metal-free catalyst and photocatalyst, benefiting from its straightforward synthesis method and enhanced activity resulting from oxygen vacancies.

4 Conclusion

In summary, WO_X nanoparticles were successfully synthesized by hydrogenating WO_3 plasma NPs, and their potential for the photodegradation of Rhodamine B (RhB) was investigated. Among the WO_X samples, $WO_{X\text{-}180}$ exhibited exceptional adsorption capacity for RhB, achieving a remarkable value of 183 mgg-1, approximately 73 times higher than that of WO_3 plasma NPs. Moreover, $WO_{X\text{-}60}$ demonstrated the highest photodegradation rate, surpassing WO_3 plasma NPs by over 90 times. These findings highlight the significant influence of reduction time on the physiochemical properties of the prepared WO_X. Besides, hydroxyl radical and photoinduced holes dominated the sites active during the photocatalytic process. This study sheds light on the impact of oxygen vacancies and expands the potential applications of WO_X as catalysts and photocatalysts to decompose various organic pollutants.

Supplementary Information The online version contains supplementary material available at https://doi.org/10.1007/s10562-024-04596-z.

Acknowledgements This study was supported by JSPS KAKENHI Grant Numbers 2670901 and 16K13642. Thank you to Annete Gabriella Nuraliya for research assisting during the review process.

Author Contributions **Osi A**: Conceptualization, data curation, methodology, investigation, original draft, writing & editing; **Aditya FA**: review & editing; **Takashi O**: review & editing; **Kikuo O**: supervising, review & editing.

Funding This article was funded by Japan Society for the Promotion of Science, 16K13642, 2670901.

Declarations

Conflict of Interest No conflict of interest for each contributing authors.

References

1. Benkhaya S, M' rabet S, El Harfi A, (2020) A review on classifications, recent synthesis and applications of textile dyes. Inorg Chem Commun 115:107891. https://doi.org/10.1016/j.inoche.2020.107891
2. Chung K-T (2016) Azo dyes and human health: A review. J Environ Sci Health C Environ Carcinog Ecotoxicol Rev 34:233–261. https://doi.org/10.1080/10590501.2016.1236602
3. Saigl ZM (2021) Various adsorbents for removal of rhodamine B dye: a review. Indones J Chem 21:1039
4. Alguacil FJ, López FA (2021) Organic dyes versus adsorption processing. Molecules 26:5440. https://doi.org/10.3390/molecules26185440
5. Al-Tohamy R, Ali SS, Li F, Okasha KM, Mahmoud YAG, Elsamahy T, Jiao H, Fu Y, Sun J (2022) A critical review on the treatment of dye-containing wastewater: Ecotoxicological and health concerns of textile dyes and possible remediation approaches for environmental safety. Ecotoxicol Environ Saf 231:113160. https://doi.org/10.1016/j.ecoenv.2021.113160
6. Lellis B, Fávaro-Polonio CZ, Pamphile JA, Polonio JC (2019) Effects of textile dyes on health and the environment and bioremediation potential of living organisms. Biotechnol Res Innov 3:275–290. https://doi.org/10.1016/j.biori.2019.09.001
7. Byrne C, Subramanian G, Pillai SC (2018) Recent advances in photocatalysis for environmental applications. J Environ Chem Eng 6:3531–3555. https://doi.org/10.1016/j.jece.2017.07.080
8. Wenderich K, Mul G (2016) Methods, mechanism, and applications of photodeposition in photocatalysis: a review. Chem Rev 116:14587–14619. https://doi.org/10.1021/acs.chemrev.6b00327
9. Anwer H, Mahmood A, Lee J, Kim K-H, Park J-W, Yip ACK (2019) Photocatalysts for degradation of dyes in industrial effluents: Opportunities and challenges. Nano Res 12:955–972. https://doi.org/10.1007/s12274-019-2287-0
10. Dutta V, Sharma S, Raizada P, Thakur VK, Khan AAP, Saini V, Asiri AM, Singh P (2021) An overview on WO_3 based photocatalyst for environmental remediation. J Environ Chem Eng 9:105018. https://doi.org/10.1016/j.jece.2020.105018
11. Wu C-M, Naseem S, Chou M-H, Wang J-H, Jian Y-Q (2019) Recent advances in tungsten-oxide-based materials and their applications. Front Mater. https://doi.org/10.3389/fmats.2019.00049
12. Koe WS, Lee JW, Chong WC, Pang YL, Sim LC (2020) An overview of photocatalytic degradation: photocatalysts, mechanisms, and development of photocatalytic membrane. Environ Sci Pollut Res 27:2522–2565. https://doi.org/10.1007/s11356-019-07193-5
13. Arutanti O, Nandiyanto ABD, Ogi T, Iskandar F, Kim TO, Okuyama K (2014) Synthesis of composite WO_3/TiO_2 nanoparticles by flame-assisted spray pyrolysis and their photocatalytic activity. J Alloys Compd. https://doi.org/10.1016/j.jallcom.2013.12.218
14. Arutanti O, Nandiyanto ABD, Ogi T, Kim TO, Okuyama K (2015) Influences of Porous Structurization and Pt Addition on the Improvement of Photocatalytic Performance of WO 3 Particles. ACS Appl Mater Interfaces 7:3009–3017. https://doi.org/10.1021/am507935j
15. Anfar Z, Zbair M, Ahsaine HA, Ezahri M, El AN (2018) Well-designed WO_3 /Activated carbon composite for Rhodamine B Removal: Synthesis, characterization, and modeling using response surface methodology. Fullerenes, Nanotub Carbon Nanostructures 26:389–397. https://doi.org/10.1080/1536383X.2018.1440386
16. Chen Q, Lou S, Wang Y, Zhou S (2023) Red blood cell-like hollow TiO_2@WO_3 microspheres as highly efficient photocatalysts for degradation of organic pollutants. Inorg Chem Commun 148:110307

17. Cuong LM, Duc BH, Van TP, Mai NTT, Chinh HD, Tu NC, Anh LTL (2021) Kinetics and adsorption model of methylene blue on g-C_3N_4@WO_3·H_2O nanoplate composite. Int J Nanosci. https://doi.org/10.1142/S0219581X21500459
18. Qamar M, Fawakhiry MO, Azad A-M, Ahmed MI, Khan A, Saleh TA (2016) Selective photocatalytic oxidation of aromatic alcohols into aldehydes by tungsten blue oxide (TBO) anchored with Pt nanoparticles. RSC Adv 6:71108–71116. https://doi.org/10.1039/C6RA11841K
19. Chen J, Qin C, Mou Y, Cao Y, Chen H, Yuan X, Wang H (2023) Linker regulation of iron-based MOFs for highly effective Fenton-like degradation of refractory organic contaminants. Chem Eng J 459:141588. https://doi.org/10.1016/j.cej.2023.141588
20. Dong P, Hou G, Xi X, Shao R, Dong F (2017) WO_3 -based photocatalysts: morphology control, activity enhancement and multifunctional applications. Environ Sci Nano 4:539–557. https://doi.org/10.1039/C6EN00478D
21. Bhavsar KS, Labhane PK, Huse VR, Dhake RB, Sonawane GH (2020) Activated carbon immobilized WO_3 nanocuboids: Adsorption/photocatalysis synergy for the enhanced removal of organic pollutants. Inorg Chem Commun 121:108215. https://doi.org/10.1016/j.inoche.2020.108215
22. El maguana Y, Elhadiri N, Benchanaa M, Chikri R, (2020) Activated carbon for dyes removal: modeling and understanding the adsorption process. J Chem 2020:1–9. https://doi.org/10.1155/2020/2096834
23. Ge J, Zhang Y, Park SJ (2019) Recent advances in carbonaceous photocatalysts with enhanced photocatalytic performances: A mini review. Materials 12:1916
24. Shang Y, Cheng X, Shi R, Ma Q, Wang Y, Yang P (2020) Synthesis and comparative investigation of adsorption capability and photocatalytic activities of WO_3 and $W_{18}O_{49}$. Mater Sci Eng B 262:114724. https://doi.org/10.1016/j.mseb.2020.114724
25. Zhu J, Wang S, Xie S, Li H (2011) Hexagonal single crystal growth of WO_3 nanorods along a [110] axis with enhanced adsorption capacity. Chem Commun 47:4403. https://doi.org/10.1039/c1cc00064k
26. Bhavani P, Kumar DP, Hussain M, Jeon K-J, Park Y-K (2022) Recent advances in wide solar spectrum active $W_{18}O_{49}$-based photocatalysts for energy and environmental applications. Catal Rev. https://doi.org/10.1080/01614940.2022.2038472
27. Xu M, Jia S, Li H, Zhang Z, Guo Y, Chen C, Chen S, Yan J, Zhao W, Yun J (2018) In-situ growth of $W_{18}O_{49}$@carbon clothes for flexible-easy-recycled photocatalysts with high performance. Mater Lett 230:224–227. https://doi.org/10.1016/j.matlet.2018.07.100
28. Shen Z, Zhao Z, Qian J, Peng Z, Fu X (2016) Synthesis of WO_{3-x} nanomaterials with controlled morphology and composition for highly efficient photocatalysis. J Mater Res 31:1065–1076. https://doi.org/10.1557/jmr.2016.106
29. Li J, Liu X, Han Q, Yao X, Wang X (2013) Formation of WO_3 nanotube-based bundles directed by $NaHSO_4$ and its application in water treatment. J Mater Chem A 1:1246–1253. https://doi.org/10.1039/C2TA00382A
30. Chen J, Ren Y, Hu T, Xu T, Xu Q (2019) Fabrication and application of substoichiometric tungsten oxide with tunable localized surface plasmon resonances. Appl Surf Sci 465:517–525
31. Liu Z, Zhang F, Li C, Inoue C (2022) Enhanced visible light response and characterization of nanoscale TiO_2/WO_{3-x} composite photocatalyst by sol–gel synthesis. Catal Letters. https://doi.org/10.1007/s10562-022-04079-z
32. Chatten R, Chadwick AV, Rougier A, Lindan PJD (2005) The oxygen vacancy in crystal phases of WO_3. J Phys Chem B 109:3146–3156. https://doi.org/10.1021/jp045655r
33. Boruah PJ, Khanikar RR, Bailung H (2020) Synthesis and characterization of oxygen vacancy induced narrow bandgap tungsten oxide (WO_{3-x}) nanoparticles by plasma discharge in liquid and its photocatalytic activity. Plasma Chem Plasma Process 40:1019–1036. https://doi.org/10.1007/s11090-020-10073-3
34. Piszcz M, Tryba B, Grzmil B, Morawski AW (2009) Photocatalytic removal of phenol under UV irradiation on WO_x–TiO_2 prepared by Sol-Gel Method. Catal Letters 128:190–196. https://doi.org/10.1007/s10562-008-9730-z
35. Rinaldi FG, Arutanti O, Arif AF, Hirano T, Ogi T, Okuyama K (2018) Correlations between reduction degree and catalytic properties of WO x nanoparticles. ACS Omega 3:8963–8970. https://doi.org/10.1021/acsomega.8b01110
36. Wang J, Liu Y, Xi X, Nie Z (2022) Microwave-assisted synthesis of hierarchical WO_3·H_2O and its selective adsorption: kinetics, isotherm and mechanism. J Mater Sci 57:6881–6899. https://doi.org/10.1007/s10853-022-06981-8
37. Putri RA, Tursiloadi S, Nurrahmah EF, Liandi AR, Arutanti O (2023) Synthesis of TiO_2-based photocatalyst from indonesia ilmenite ore for photodegradation of eriochrome Black-T Dye. Water Air Soil Pollut. https://doi.org/10.1007/s11270-023-06584-2
38. Springsteen A (2001) Colour and the optical properties of materials. Color Res Appl 26:103–103
39. Zhang L, Wang H, Liu J, Zhang Q, Yan H (2020) Nonstoichiometric tungsten oxide: structure, synthesis, and applications. J Mater Sci Mater Electron 31:861–873. https://doi.org/10.1007/s10854-019-02596-z
40. Bandi S, Srivastav AK (2021) Review: Oxygen-deficient tungsten oxides. J Mater Sci 56:6615–6644. https://doi.org/10.1007/s10853-020-05757-2
41. Subhiksha V, Kokilavani S, Sudheer Khan S (2022) Recent advances in degradation of organic pollutant in aqueous solutions using bismuth based photocatalysts: A review. Chemosphere 290:133228. https://doi.org/10.1016/j.chemosphere.2021.133228
42. Mulliken RS (1934) A new electroaffinity scale; Together with data on valence states and on valence ionization potentials and electron affinities. J Chem Phys. https://doi.org/10.1063/1.1749394
43. Mulliken RS (1935) Electronic structures of molecules XI. Electroaffinity, molecular orbitals and dipole moments. J Chem Phys. https://doi.org/10.1063/1.1749731
44. Tang X, Huang J, Liao H, Chen G, Mo Z, Ma D, Zhan R, Li Y, Luo J (2019) Growth of $W_{18}O_{49}$/WO:X/W dendritic nanostructures by one-step thermal evaporation and their high-performance photocatalytic activities in methyl orange degradation. CrystEngComm. https://doi.org/10.1039/c9ce01047e
45. Liu T, Wang L, Lu X, Fan J, Cai X, Gao B, Miao R, Wang J, Lv Y (2017) Comparative study of the photocatalytic performance for the degradation of different dyes by ZnIn2S4: adsorption, active species, and pathways. RSC Adv. https://doi.org/10.1039/c7ra00199a

Authors and Affiliations

Osi Arutanti[1,3] · Aditya Farhan Arif[2,3] · Takashi Ogi[4] · Kikuo Okuyama[4]

✉ Osi Arutanti
osi.arutanti@brin.go.id

[1] Research Center for Chemistry, National Research and Innovation Agency, Gd. 452 KST BJ Habibie, Tanggerang Selatan, Serpong, Indonesia

[2] Corporate Strategy, PT Mineral Industri Indonesia (Persero), MIND ID, Jakarta, Indonesia

[3] Research Collaboration Center for Advanced Energy Materials, Jalan Ganesha 10, Bandung, West Java 40132, Indonesia

[4] Department of Chemical Engineering, Graduate School of Engineering, Hiroshima University, 1-4-1 Kagamiyama, Higashi, Hiroshima 739-8527, Japan